

REPORT DOCUMENTATION PAGE			Form Approved OMB NO. 0704-0188		
<p>The public reporting burden for this collection of information is estimated to average 1 hour per response, including the time for reviewing instructions, searching existing data sources, gathering and maintaining the data needed, and completing and reviewing the collection of information. Send comments regarding this burden estimate or any other aspect of this collection of information, including suggestions for reducing this burden, to Washington Headquarters Services, Directorate for Information Operations and Reports, 1215 Jefferson Davis Highway, Suite 1204, Arlington VA, 22202-4302. Respondents should be aware that notwithstanding any other provision of law, no person shall be subject to any penalty for failing to comply with a collection of information if it does not display a currently valid OMB control number.</p> <p>PLEASE DO NOT RETURN YOUR FORM TO THE ABOVE ADDRESS.</p>					
1. REPORT DATE (DD-MM-YYYY) 21-03-2015		2. REPORT TYPE Final Report		3. DATES COVERED (From - To) 1-Oct-2006 - 30-Nov-2012	
4. TITLE AND SUBTITLE Final Report: Reduced-Volume Fracture Toughness Characterization for Transparent Polymers			5a. CONTRACT NUMBER		
			5b. GRANT NUMBER W911NF-04-D-0001		
			5c. PROGRAM ELEMENT NUMBER 611102		
6. AUTHORS David M. Stepp			5d. PROJECT NUMBER		
			5e. TASK NUMBER		
			5f. WORK UNIT NUMBER		
7. PERFORMING ORGANIZATION NAMES AND ADDRESSES Duke University 2200 W Main Street Suite 710 Erwin Square Durham, NC 27705 -4677			8. PERFORMING ORGANIZATION REPORT NUMBER		
9. SPONSORING/MONITORING AGENCY NAME(S) AND ADDRESS (ES) U.S. Army Research Office P.O. Box 12211 Research Triangle Park, NC 27709-2211			10. SPONSOR/MONITOR'S ACRONYM(S) ARO		
			11. SPONSOR/MONITOR'S REPORT NUMBER(S) 50952-MS-SR.3		
12. DISTRIBUTION AVAILABILITY STATEMENT Approved for Public Release; Distribution Unlimited					
13. SUPPLEMENTARY NOTES The views, opinions and/or findings contained in this report are those of the author(s) and should not be construed as an official Department of the Army position, policy or decision, unless so designated by other documentation.					
14. ABSTRACT The research effort has made significant progress, both experimentally and computationally. A consistent approach was established to reliably measure the fracture toughness of very small volumes of transparent engineering polymers, utilizing photo elasticity to minimize the amount of retained stress in small samples and assure local stress concentrations were not affecting the measurements. A unique cohesive zone model was developed to simulate the ductile to brittle failure transition in polycarbonate. The model is formulated so that as rate or stress state changes within a simulation, the fracture energy and thus fracture mode may also change appropriately. The					
15. SUBJECT TERMS polycarbonate fracture ductile brittle transition					
16. SECURITY CLASSIFICATION OF:			17. LIMITATION OF ABSTRACT UU	15. NUMBER OF PAGES	19a. NAME OF RESPONSIBLE PERSON David Stepp
a. REPORT UU	b. ABSTRACT UU	c. THIS PAGE UU			19b. TELEPHONE NUMBER 919-549-4329

Report Title

Final Report: Reduced-Volume Fracture Toughness Characterization for Transparent Polymers

ABSTRACT

The research effort has made significant progress, both experimentally and computationally. A consistent approach was established to reliably measure the fracture toughness of very small volumes of transparent engineering polymers, utilizing photo elasticity to minimize the amount of retained stress in small samples and assure local stress concentrations were not affecting the measurements. A unique cohesive zone model was developed to simulate the ductile to brittle failure transition in polycarbonate. The model is formulated so that as rate or stress state changes within a simulation, the fracture energy and thus fracture mode may also change appropriately. The ductile to brittle transition occurs when the cohesive opening rate is greater than a threshold opening rate and when the stress state is close to plane strain in a fracture specimen. These effects are coupled in a phenomenological model, and the transition from slow to fast crack growth can be captured, even as test loading rate and/or sample thickness are varied, by using a single set of bulk and cohesive zone material parameters.

Enter List of papers submitted or published that acknowledge ARO support from the start of the project to the date of this printing. List the papers, including journal references, in the following categories:

(a) Papers published in peer-reviewed journals (N/A for none)

<u>Received</u>	<u>Paper</u>
-----------------	--------------

TOTAL:

Number of Papers published in peer-reviewed journals:

(b) Papers published in non-peer-reviewed journals (N/A for none)

<u>Received</u>	<u>Paper</u>
-----------------	--------------

TOTAL:

Number of Papers published in non peer-reviewed journals:

(c) Presentations

2011 USNCCM: "Predicting the Transition from Ductile to Brittle Failure in Polycarbonate"

2011 IESE Talk: "The Ductile to Brittle Transition in Polycarbonate"

Number of Presentations: 2.00

Non Peer-Reviewed Conference Proceeding publications (other than abstracts):

Received Paper

TOTAL:

Number of Non Peer-Reviewed Conference Proceeding publications (other than abstracts):

Peer-Reviewed Conference Proceeding publications (other than abstracts):

Received Paper

TOTAL:

Number of Peer-Reviewed Conference Proceeding publications (other than abstracts):

(d) Manuscripts

Received Paper

TOTAL:

Number of Manuscripts:

Books

Received Book

TOTAL:

Received Book Chapter

TOTAL:

Patents Submitted

Patents Awarded

Awards

Graduate Students

<u>NAME</u>	<u>PERCENT SUPPORTED</u>	Discipline
Justin Pogacnik	1.00	
FTE Equivalent:	1.00	
Total Number:	1	

Names of Post Doctorates

<u>NAME</u>	<u>PERCENT SUPPORTED</u>
FTE Equivalent:	
Total Number:	

Names of Faculty Supported

<u>NAME</u>	<u>PERCENT SUPPORTED</u>	National Academy Member
John Dolbow	0.04	
FTE Equivalent:	0.04	
Total Number:	1	

Names of Under Graduate students supported

<u>NAME</u>	<u>PERCENT SUPPORTED</u>
FTE Equivalent:	
Total Number:	

Student Metrics

This section only applies to graduating undergraduates supported by this agreement in this reporting period

The number of undergraduates funded by this agreement who graduated during this period: 0.00

The number of undergraduates funded by this agreement who graduated during this period with a degree in science, mathematics, engineering, or technology fields:..... 0.00

The number of undergraduates funded by your agreement who graduated during this period and will continue to pursue a graduate or Ph.D. degree in science, mathematics, engineering, or technology fields:..... 0.00

Number of graduating undergraduates who achieved a 3.5 GPA to 4.0 (4.0 max scale):..... 0.00

Number of graduating undergraduates funded by a DoD funded Center of Excellence grant for Education, Research and Engineering:..... 0.00

The number of undergraduates funded by your agreement who graduated during this period and intend to work for the Department of Defense 0.00

The number of undergraduates funded by your agreement who graduated during this period and will receive scholarships or fellowships for further studies in science, mathematics, engineering or technology fields: 0.00

Names of Personnel receiving masters degrees

<u>NAME</u>
Total Number:

Names of personnel receiving PHDs

<u>NAME</u>
Justin Pogacnik
Total Number:

Names of other research staff

<u>NAME</u>	<u>PERCENT SUPPORTED</u>
FTE Equivalent:	
Total Number:	

Sub Contractors (DD882)

Inventions (DD882)

Scientific Progress

See attachment.

Technology Transfer

None.

New Rate and Stress Dependent Cohesive Zone Model for Simulating the Ductile to Brittle Failure Transition in Polycarbonate

Justin Pogacnik^{a,1,*}, Martin Hautefeuille^a, John Dolbow^a, David Stepp^{b,a}, George Pearsall^a

^aPratt School of Engineering, Duke University, Durham, NC 27705, USA

^bU.S. Army Research Office, Research Triangle Park, NC 27709, USA

Abstract

A new cohesive zone model is developed to simulate the ductile to brittle failure transition in polycarbonate. The model is formulated so that as rate or stress state changes within a simulation, the fracture energy and thus fracture mode may also change appropriately. The ductile to brittle transition occurs when the cohesive opening rate is greater than a threshold opening rate and when the stress state is close to plane strain in a fracture specimen. These effects are coupled in a phenomenological model. The principal contribution of this work is that, in a glassy polymer, the transition from slow to fast crack growth as test loading rate and/or sample thickness are varied can be simulated by using a single set of bulk and cohesive zone material parameters. This result enlists the use of the Simplified Potential Energy Clock (SPEC) model and the new cohesive zone model with rate and stress-state dependencies in three-dimensional finite element analysis.

1. Introduction

Engineering thermoplastic polymers are used in a variety of applications. Polycarbonate (PC) is a transparent engineering polymer noted for its toughness. Other transparent amorphous polymers, like polymethyl methacrylate (PMMA) and polystyrene (PS), exhibit more brittle failure than PC. Because of polycarbonate's toughness, it is useful for applications such as protective visors, goggles, helicopter canopies, automotive headlight lenses, helmets, drinking bottles, riot shields, *etc.* Though PC exhibits greater toughness than other transparent amorphous polymers, it is subject to catastrophic failure in the presence of a flaw. In fact, its impact fracture strength in the presence of a sharp crack falls into the range that is typical of many common polymers. Since PC is used in protective-type applications, catastrophic failures can be hazardous to the individuals involved.

In mode I loading, polycarbonate can fail in one of two ways: ductile or brittle. Hull and Owen (1973) were the first to characterize the fracture surface morphology of the two failure types. Ductile failure can be described as a "tearing" type of failure with significant plastic deformation and a high amount of energy required for failure. When glassy polymers are loaded under certain conditions (i.e., plane-stress or in uniaxial compression), they exhibit shear yielding. Shear yielding is a bulk process associated with ductile failure. In brittle failure, crack growth occurs rapidly with little macroscopic deformation and energy dissipation. Under certain tensile conditions (i.e., plane-strain or faster strain rates), many polymers fail in a brittle manner. Brittle failure is often associated with crazing in the material (Kambour (1973), Ishikawa et al. (1977), Kramer (1984), and Estevez et al. (2000)). The ductile to brittle transition in glassy polymers is typically viewed as a competition between shear yielding and crazing. Crazing is a micro-mechanical process where polymer chains align in the direction of the maximum principal stress. Kramer (1984) provides a comprehensive treatise on the crazing process. Work performed by Wolstenholme et al. (1964),

Ravetti et al. (1975), Broutman and Krishnakumar (1976), Yee (1977), and Selden (1987) indicate that polycarbonate (and some other glassy polymers) actually have two distinct energy release rates associated with mode I crack growth. The lower (or critical) value is associated with fast, unstable fracture, while a higher threshold value exists that is associated with slower, ductile and potentially stable crack growth. Some conditions that can lead to a transition from one failure energy to the other include loading rate, test temperature, plastic zone size, specimen thickness (i.e., plane-stress or plane-strain stress state), and notch sharpness.

Commonly used approaches for simulating failure with finite elements can include implicit approaches (like the X-FEM approach introduced by Moes et al. (1999)), hybrid methods like an element deletion technique, and explicit approaches that use cohesive elements. Implicit approaches utilizing the X-FEM typically enforce a failure criterion that results in element enrichment to model crack growth. The method can be desirable because exact theoretical solutions can be exactly matched. Sample failure criteria could be critical crack tip opening displacement (CTOD) or critical stress intensity factor (K_{IC}). These techniques have been used with great success, but can quickly become overly complex in three dimensional analyses. An element deletion technique was used by Gearing and Anand (2004) to model failure in glassy polymers. Element deletion is typically used in finite strain analyses when elements can become distorted and bulk processes control failure. Mass and energy conservation can cause error accumulation when using element deletion techniques. Explicit techniques that utilize cohesive zone elements have been used with considerable success for modeling failure. The works of Tjssens et al. (2000), Estevez et al. (2000) introduce a rate and temperature dependent cohesive zone for crazing in glassy polymer failure. Anvari et al. (2006) introduce a rate and stress-dependent cohesive zone model designed for failure in metals. Models based on this work have been successfully applied in 2D quasi-static investigations of ductile failure by Banerjee and Manivasagam (2009) and Scheider et al. (2011).

Caruthers et al. (2004) developed a thermodynamically consistent, nonlinear viscoelastic bulk constitutive model based on a potential energy clock (PEC) for modeling polymer deformations. It relies on the assumption that all polymer relaxation rates depend on the potential energy of the system. Typically, polymers are modeled with hyperelastic, plasticity, or viscoelastic models. The models can give similar results under certain circumstances, but the physical differences are significant. Glassy polymers do exhibit a linear viscoelastic response that does not significantly change with temperature except that relaxation times change. Because of its formulation, the PEC model predicts mechanical yield as a natural consequence of relaxation behavior induced by loading. Plasticity models predict yield, but need a second mechanism to describe the glass transition. Hyperelastic models do show a softening type of behavior, but hysteresis effects are not naturally accounted for. Adolf et al. (2009) developed a method of simplifying the PEC model to create a more usable constitutive model for general engineering analyses. They termed the model the Simplified PEC model or SPEC. The main contributions of the SPEC model were to create a formulation that was simpler to parameterize and implement computationally. The model was shown by Adolf et al. (2009) to successfully capture the time and temperature dependent behavior of polymers. It is attractive because one set of material parameters can predict a wide range of material behaviors like stress relaxation, yield, volume relaxation after quenching into glass, and physical aging for both thermoplastic and thermoset polymers.

In this work, a new cohesive zone model is developed and implemented to simulate the ductile to brittle failure transition in polycarbonate. The model is rate and stress-state dependent and accounts for both the high and low energy failure modes associated with ductile and brittle failure, respectively. The rate dependence of the model is capable of capturing the failure mode transition due to changes in the external loading rate. The stress-state dependence of the model is capable of capturing the failure mode transition due to thickness effects, i.e., plane-strain or plane-stress. For the first time, these effects are coupled in a way that a consistent set of parameters can be used to simulate the transition from ductile to brittle failure in a glassy polymer due to either or both of these effects. The CZM is based on the simple model introduced by Tvergaard and Hutchinson (1992) but allows for two distinct energies per unit area of crack growth: 1) a high energy case associated with ductile failure and slow crack growth and 2) a low energy case associated with brittle failure and fast crack growth. This is important because polycarbonate does not show a continuous transition in failure energy as loading rate or stress state change. Rather, an abrupt transition occurs from high to low energy failure at a critical point. The discrete manner of this implementation naturally lends itself to simulation using explicit dynamics. It is also important to recognize that a robust bulk constitutive model is necessary to capture the failure transition because in ductile failure, high amounts of energy are dissipated through bulk processes. A cohesive zone model is used, in this analysis, to simply enforce the appropriate energetic and bulk response for failure based on empirical evidence of strain-rate and stress-state effects.

First, the form of the SPEC model used for this study will be outlined in Section 2. The new CZM developed for this work will be presented in Section 3. Section 4 will present the finite element method and the initial boundary value problem used in this work. Section 5 will present the numerical experiments performed to demonstrate the problem set-up for mode-I fracture simulations for the single edge-notch tension (SENT) specimen geometry and the results of those analyses. The final section will conclude with a discussion of the findings of this study and a summary of the contributions.

2. Bulk Constitutive Model - Simplified Potential Energy Clock (SPEC)

Glassy polymers behave in a nonlinear viscoelastic manner that is also temperature-dependent. Polymer relaxation rates diminish as the test temperature decreases below the glass transition temperature, T_g . Generally, viscoelastic and viscoplastic models lack the robustness to describe a full range of polymer behaviors such as stress relaxation, yield under constant strain rate loading, volume relaxation after quenching into glass, and physical aging (see Caruthers et al. (2004) and Adolf et al. (2009)).

The following is a brief summary of the PEC and SPEC models. Readers are referred to Caruthers et al. (2004) and Adolf et al. (2009) for the full theoretical development of those models. The PEC and SPEC models begin with the expansion of the Helmholtz free energy Ψ about an equilibrium state that would exist at the current temperature T and density ρ .

$$\begin{aligned}\Psi &= \Psi_{eq}(T, \underline{\underline{H}}) \\ &+ \frac{1}{2}\Psi_1 \int_0^t \int_0^t ds du f_1(t^* - s^*, t^* - u^*) \frac{dI_1}{ds} \frac{dI_1}{du} \\ &+ \Psi_2 \int_0^t \int_0^t ds du f_2(t^* - s^*, t^* - u^*) \frac{dH}{ds} : \frac{dH}{du} \\ &+ \Psi_3 \int_0^t \int_0^t ds du f_3(t^* - s^*, t^* - u^*) \frac{dT}{ds} \frac{dI_1}{du} \\ &+ \frac{1}{2}\Psi_4 \int_0^t \int_0^t ds du f_4(t^* - s^*, t^* - u^*) \frac{dT}{ds} \frac{dT}{du}\end{aligned}\tag{1}$$

where $\underline{\underline{H}}$ is the Hencky strain measure, which is a logarithmic strain measure, and I_1 is its first invariant that is a function of volume only. This avoids volumetric inconsistencies that can arise with other strain measures. The prefactors Ψ_{1-4} depend on the current strain and temperature and are related to, though not necessarily equal to the bulk modulus K , the shear modulus G , the coefficient of thermal expansion α , and the specific heat capacity at a constant volume C_v , respectively. The functions f_{1-4} are relaxation functions dependent on the ‘material time’, t^* , that is dependent on the potential energy of the system, E^{pot} , that can be described by a generalized Williams-Landel-Ferry (WLF) equation

$$t^* - s^* = \int_s^t \frac{dx}{a(x)},\tag{2}$$

where

$$\log a = -C_1 \left[\frac{E^{pot} - E_{ref}^{pot}}{C'_2 + E^{pot} - E_{ref}^{pot}} \right],\tag{3}$$

where C_1 is the first WLF constant and C'_2 is related to the second WLF constant. The first Piola-Kirchhoff stress can be calculated by

$$\underline{\underline{S}} = \rho_{ref} \left(\frac{\partial \Psi}{\partial \underline{\underline{H}}} \right)_T : \frac{d\underline{\underline{H}}}{d\underline{\underline{E}}},\tag{4}$$

where $\underline{\underline{E}}$ is the Green-Lagrange strain measure¹. The Cauchy stress can be found in the usual way, $\underline{\underline{\sigma}} = (\rho/\rho_{ref}) \underline{\underline{F}} \cdot \underline{\underline{S}} \cdot \underline{\underline{F}}^T$, where $\underline{\underline{F}}$ is the deformation gradient which can be broken down into rotated and unrotated or rotation and stretch components as

$$\underline{\underline{F}} = \underline{\underline{R}} \cdot \underline{\underline{U}}. \quad (5)$$

The use of the Hencky strain measure requires the calculation of a logarithmic strain measure and a fourth-order tensor for the Piola-Kirchhoff stress (see (4)). In order to simplify these calculations, the SPEC model utilizes an approximation of the Hencky strain rate by the unrotated rate of deformation tensor, $\underline{\underline{d}}$

$$\underline{\underline{d}} = \frac{1}{2} \left[\underline{\underline{U}}^{-1} \cdot \frac{d\underline{\underline{U}}}{dt} + \frac{d\underline{\underline{U}}}{dt} \cdot \underline{\underline{U}}^{-1} \right]. \quad (6)$$

If the approximate stress associated with $\underline{\underline{d}}$ is called $\underline{\underline{\sigma}}_d$, then the Cauchy stress can be calculated by

$$\underline{\underline{\sigma}} = \frac{\rho}{\rho_{ref}} \underline{\underline{R}} \cdot \underline{\underline{\sigma}}_d \cdot \underline{\underline{R}}^T. \quad (7)$$

In order to arrive at the final Cauchy stress to be used in calculations, the Hencky strain of (1) is replaced by $\underline{\underline{d}}$. The model prefactors Ψ_{1-4} are assumed to be constant so that they take on relationships to the physical quantities discussed earlier. Finally, the relaxation functions f_{1-4} are replaced with either f_v or f_s which stand for volumetric and shear relaxation functions. The general relaxation functions are either related to volumetric quantities (bulk modulus, coefficient of thermal expansion, and specific volumetric heat capacity) or a shear quantity (i.e., shear modulus). Adolf et al. (2009) state that in previous parameterizations, the volumetric relaxations differed very little and could be lumped into a single relaxation function. The final Cauchy stress is expressed by

$$\begin{aligned} \underline{\underline{\sigma}} &= \frac{\rho}{\rho_{ref}} \left[K_d(T) \int_0^t ds f_v(t^* - s^*) \frac{dI_1}{ds} \right. \\ &\quad \left. - L_d(T) \int_0^t ds f_v(t^* - s^*) \frac{dT}{ds} \right] \underline{\underline{I}} \\ &\quad + \frac{2\rho G_d(T)}{\rho_{ref}} \int_0^t ds f_s(t^* - s^*) \times \left[\underline{\underline{R}}(t) \cdot \underline{\underline{d}}_{dev} \cdot \underline{\underline{R}}(t)^{-1} \right] \\ &\quad + \frac{\rho}{\rho_{ref}} \left[K_\infty(T) I_1 - L_\infty(T) \{T - T_{ref}\} \right] \underline{\underline{I}} \\ &\quad + \frac{2\rho G_\infty(T)}{\rho_{ref}} \left[\underline{\underline{R}} \cdot \underline{\underline{\varepsilon}}_{dev} \cdot \underline{\underline{R}}^{-1} \right], \end{aligned} \quad (8)$$

where $(\cdot)_d = (\cdot)_g - (\cdot)_\infty$ is the difference between a material value in the glassy state and in the rubbery state, the product of the bulk modulus and the coefficient of thermal expansion is expressed as $L = K\alpha$, and $\underline{\underline{\varepsilon}}_{dev}$ is the deviatoric part of the integrated rate of deformation tensor. For completeness, (3) can be recast as

$$\log a = -\frac{C_1 N}{C_2'' + N}, \quad (9)$$

where

$$C_2'' = C_2 \left[1 + C_3 \alpha_\infty^{ref} \right] \cong C_2 \left[1 + \frac{T_{ref} L_d^{ref} \alpha_\infty^{ref}}{\rho_{ref} C_{vd}^{ref}} \right], \quad (10)$$

where C_2 is the second WLF coefficient and

$$N = \left[\{T - T_{ref}\} - \int_0^t ds f_v(t^* - s^*) \frac{dT}{ds} \right]$$

¹ $\underline{\underline{E}}$ is a tensor quantity that is distinct from the scalar E^{pot} used in (3).

$$\begin{aligned}
& + C_3 \left[I_1 - \int_0^t ds f_v(t^* - s^*) \frac{dI_1}{ds} \right] \\
& + C_4 \int_0^t \int_0^t ds du f_s(t^* - s^*, t^* - u^*) \frac{d}{\equiv_{dev}}(s) : \frac{d}{\equiv_{dev}}(u),
\end{aligned} \tag{11}$$

where

$$C_3 \approx \frac{T_{ref} L_d^{ref}}{\rho_{ref} C_{vd}^{ref}}, \tag{12}$$

and

$$C_4 \approx - \frac{G_d^{ref}}{\rho_{ref} C_{vd}^{ref}}. \tag{13}$$

C_3 and C_4 are clock constants that describe the dependence of relaxation times on volume and applied deformations. C_3 produces an apparent glass transition temperature with pressure and C_4 produces yield. The volumetric and shear relaxation functions take the form of a stretched exponential function

$$f_{v,s}(t) = \exp \left[- \left(\frac{t}{\tau_{v,s}} \right)^{\beta_{v,s}} \right], \tag{14}$$

where τ and β are the constants of the relaxation function that need to be determined through experiment.

3. Cohesive Zone Model Development

3.1. Introduction to CZMs

In order to introduce cohesive zone models, it is first beneficial to introduce the concept of cohesive failure. Zhang et al. (2007) offer a clear explanation of CZM theory. At the crack tip, materials cannot sustain theoretical infinite stress values associated with the stress singularity. The material softens in the crack tip regions where it is also subject to various micromechanical processes such as microvoid formation, micro-cracking, polymer chain orientation, and/or crazing. This softening can be simulated by a traction-separation law acting in the cohesive zone in a plane along the path of potential crack propagation. The theory of cohesive zones was first introduced by Barenblatt (1959) and Dugdale (1960) as a plastic strip yield model. Within the cohesive zone, the material separates to a distance Δ_{coh}^α as a result of the stresses acting near the crack tip. The superscript α is used to indicate the component of the traction tensor of interest. $\alpha = \{n, t_1, t_2\}$ for the normal component of displacement and the two tangential components t_1 and t_2 , respectively. The cohesive zone surface sustains a distribution of tractions $\hat{\sigma}_{coh}^\alpha$, which are functions of the displacement jump across the surface Δ_{coh}^α . The relationship between $\hat{\sigma}_{coh}^\alpha$ and Δ_{coh}^α is defined as the constitutive law for the cohesive zone surface.

3.2. Model Background

The cohesive zone constitutive law used in this work is derived from the model presented by Tvergaard and Hutchinson (1992). Figure 2 displays the traction-separation behavior of that model referred to as the TH model. In the model, δ_1^α , δ_2^α , and δ_c^α are shape parameters that are bounded by $0 \leq \delta^\alpha \leq 1$ where

$$\delta_c^\alpha = \frac{\Delta_{coh}^\alpha}{\Delta_p^\alpha} = 1. \tag{15}$$

Cohesive failure occurs when the normal cohesive opening is greater than or equal to the peak normal cohesive opening, i.e., $\Delta_{coh}^\alpha \geq \Delta_p^\alpha$. The traction response is calculated by a piecewise function as

$$\hat{\sigma}_{coh}^\alpha = \begin{cases} \frac{\hat{\sigma}_p^\alpha}{\delta_1^\alpha \Delta_p^\alpha} \Delta_{coh}^\alpha & \text{for } \Delta_{coh}^\alpha \leq \delta_1^\alpha \Delta_p^\alpha \\ \hat{\sigma}_p^\alpha & \text{for } \delta_1^\alpha \Delta_p^\alpha < \Delta_{coh}^\alpha < \delta_2^\alpha \Delta_p^\alpha \\ \hat{\sigma}_p^\alpha \left(\frac{1}{1 - \delta_2^\alpha} \right) \left[1 - \frac{\Delta_{coh}^\alpha}{\Delta_p^\alpha} \right] & \text{for } \delta_2^\alpha \Delta_p^\alpha \leq \Delta_{coh}^\alpha \leq \Delta_p^\alpha \end{cases}, \tag{16}$$

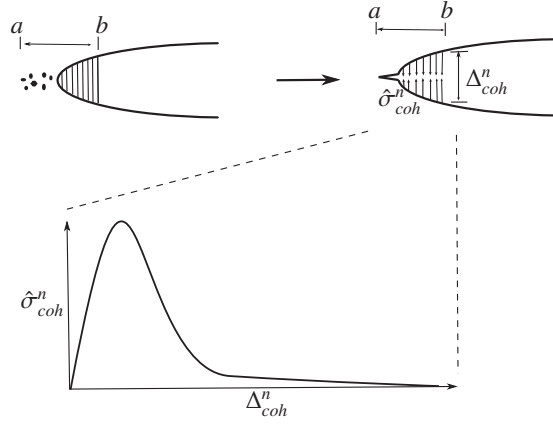


Figure 1: Generic cohesive zone description (adapted from Zhang et al. (2007) and Barenblatt (1959)). On the top left, micro-mechanical processes are depicted as micro void formation and crazing. These are idealized as a fracture process zone from a to b where a traction-separation law controls the normal opening behavior in that region.

where $0 < \delta_1^\alpha < \delta_2^\alpha < 1$ because the separation value of the cohesive zone is normalized by the maximum separation Δ_p^α .

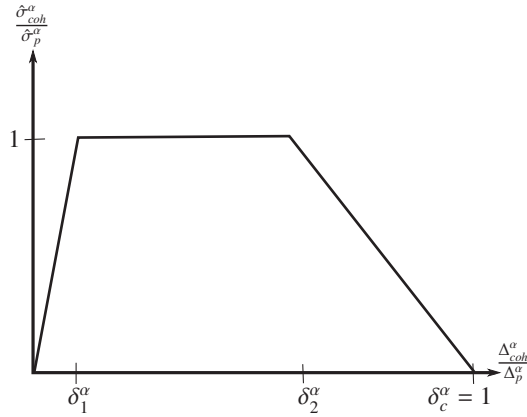


Figure 2: Traction-separation law from Tvergaard and Hutchinson (1992).

Tvergaard and Hutchinson (1992) show that the work of separation per unit area which is found by calculating the area under the traction-separation curve is given by:

$$\begin{aligned}
 W_0 &= \int_0^{\Delta_p^n} \hat{\sigma}_{coh}^n d\Delta_{coh}^n \\
 &= \frac{1}{2} \hat{\sigma}_p^n \Delta_p^n (\delta_c^n + \delta_2^n - \delta_1^n).
 \end{aligned} \tag{17}$$

3.3. Failure Energy

As stated earlier, polycarbonate (and some other glassy polymers) actually have two distinct energy release rates associated with crack growth. The lower (or critical) value is associated with fast, unstable fracture, while a higher threshold value exists that is associated with slower, ductile and potentially stable crack growth. In examining the transition from ductile to brittle failure, it is necessary to formulate a cohesive zone model that will account for both

energy requirements simultaneously. That is, the cohesive zone model must require high amounts of energy in some instances, but also be capable of capturing the worst-case (minimal energy) scenario for crack growth.

Figure 3 demonstrates the normal direction traction-separation behavior of the new cohesive zone model and (18) displays the traction-separation equation.

$$\hat{\sigma}_{coh}^{\alpha} = \begin{cases} \frac{\hat{\sigma}^{\alpha}}{\delta_1^{\alpha}} \Delta_{coh}^{\alpha} & \text{for } \Delta_{coh}^{\alpha} \leq \delta_1^{\alpha} \Delta^{\alpha} \\ \hat{\sigma}^{\alpha} & \text{for } \delta_1^{\alpha} \Delta^{\alpha} < \Delta_{coh}^{\alpha} < \delta_2^{\alpha} \Delta^{\alpha} \\ \hat{\sigma}^{\alpha} \left(\frac{1}{1-\delta_2^{\alpha}} \right) \left[1 - \frac{\Delta_{coh}^{\alpha}}{\Delta^{\alpha}} \right] & \text{for } \delta_2^{\alpha} \Delta^{\alpha} \leq \Delta_{coh}^{\alpha} \leq \Delta^{\alpha} \end{cases} \quad (18)$$

In the high energy case, the normal direction components are $\Delta^n = \Delta_{max}$ and $\hat{\sigma}^n = \hat{\sigma}_{max}$ and in the lower energy (or critical) case, $\Delta^n = \Delta_{min}$ and $\hat{\sigma}^n = \hat{\sigma}_{min}$. Two different energy values are possible depending on the fracture mode (ductile or brittle). In the tangential directions, $\hat{\sigma}^{t1} = \hat{\sigma}^{t2} = \hat{\sigma}_{min}$ and $\Delta^{t1} = \Delta^{t2} = \Delta_{min}$. The tangential direction model parameters could be adjusted for a more general loading scenario, but the minimum values of the normal direction were used since only mode I loading was considered in this work. The remainder of this section will focus on the normal opening direction of the cohesive zone model, since it is the most important in mode I loading.

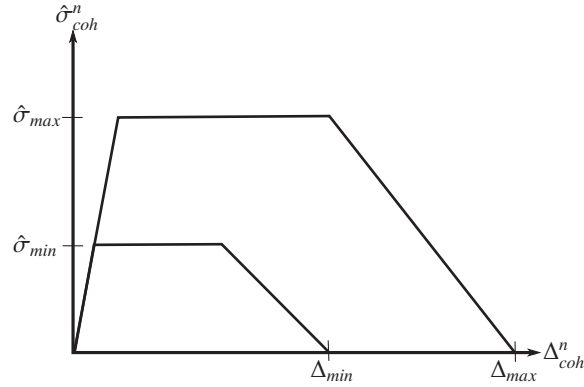


Figure 3: Normal traction-separation behavior of new cohesive zone model. Two distinct traction-separation behaviors are possible depending on the expected fracture mode (ductile or brittle).

In this work, two factors were used to determine which traction-separation curve was used: normalized cohesive zone opening rate and the stress state of the surrounding bulk material. The mode I cohesive zone opening rate is directly influenced by the test loading rate. The stress state of the surrounding material is directly influenced by the specimen thickness. The limits of the stress state are represented as plane-stress and plane-strain scenarios; however, three-dimensional problems will represent a range of stress states somewhere between the limits. Figure 4 shows how the cohesive energy E_{coh} for failure changes when either the cohesive opening rate or the stress state in the surrounding material reach critical levels: λ_C and σ_{RC} , respectively. σ_R is a stress ratio related to the amount of plane strain present. It will be defined more rigorously in Sections 3.5 and 3.6.

3.4. Rate Dependence

Consider Figure 4 in the case of rate controlled failure. If the relative opening rate λ is slow, the higher energy traction-separation law will dominate. Alternatively, if the relative opening rate is fast, the lower energy traction-separation law will dominate the behavior. If the loading rate fluctuates, the law is free to move between the two energy values and thus, the two curves of Figure 3.

For a given time t , that is updated to a new time $t + dt$ over a time step of size dt , the normalized cohesive opening rate over dt is calculated as

$$\lambda = \frac{\Delta_{t+dt}^n - \Delta_t^n}{\Delta_p^n \cdot dt}, \quad (19)$$

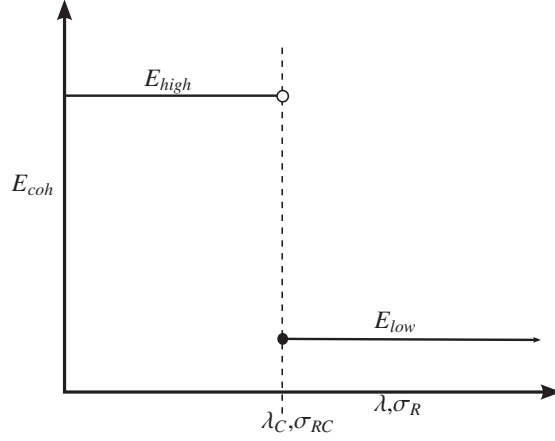


Figure 4: Cohesive energy as a function of cohesive opening rate or stress state. Higher opening rates or higher stress states (plane-strain) result in lower energy requirements for failure.

where Δ_t^n represents the cohesive separation at time t and Δ_p^n is the peak separation resulting in failure of the cohesive zone and can be either Δ_{min} or Δ_{max} depending on the energy required for failure. λ is divided by the time step in order to account for changes in the amount of opening that can occur because of changes in the time step. That is, in a large time step, more opening can occur, while the rate of opening is actually the same. This is how the separation rate was calculated in this work to determine the controlling traction-separation curve. The model parameter λ_C can be adjusted to capture the failure behavior seen in experiments at different loading rates.

3.5. Stress-State Dependence

The stress-state of the material ahead of the crack front affects crack propagation. In standard ASTM-designated fracture toughness testing, the thickness of the sample must be large enough to constrain deformation in the thickness direction (predominantly plane-strain situation) and result in a minimal amount of energy required for failure. At least one example of a stress-state dependent cohesive zone has been implemented by Anvari et al. (2006), their work was performed on two-dimensional plane-strain models. However, Section 5.4.1 will show that three-dimensional analysis is beneficial in analyzing the plane-strain/plane-stress condition.

Figure 5 represents a planar crack in an arbitrary domain. Assume the loading is mode I; therefore, the loading direction y' should be orthogonal to the crack propagation direction x' and in the same direction as the maximum principal stress. Therefore, for a Cartesian coordinate system, the last coordinate direction z' will be the direction that is orthonormal to the plane $x'y'$. The component of the stress tensor acting in the z' direction is the component of interest, since this is the out of plane stress associated with the plane stress or plane strain condition. It is desirable to perform the cohesive zone stress analysis in the $\{x', y', z'\}$ space. However, the stress tensor is usually expressed in terms of the global coordinate space $\{x, y, z\}$. A standard coordinate transformation can be used to relate the global stress tensor σ_{ij} to the crack-oriented stress tensor σ'_{km} expressed as

$$\sigma'_{km} = \sigma_{ij} \frac{\partial x'_k}{\partial x_j} \frac{\partial x'_m}{\partial x_i} = \sigma_{ij} \beta_{kj} \beta_{mi}, \quad (20)$$

where $\beta_{kj} = \cos(x'_k, x_j)$ is the cos of the x'_k axis with respect to the x_j axis.

Since the in-plane components remain relatively constant, an appropriate value to determine the relative magnitude of the thickness-direction stresses is

$$\sigma_R = \frac{\sigma'_{zz}}{\sigma'_{xx} + \sigma'_{yy}}, \quad (21)$$

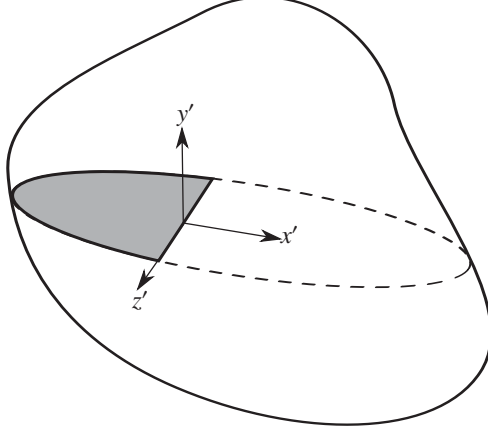


Figure 5: Planar crack in an arbitrary domain.

where σ_R is the bulk stress ratio mentioned in Section 3.3. This ratio is especially convenient for analysis, since from the generalized Hooke's law in the plane-strain case,

$$\sigma'_{zz} = \nu (\sigma'_{xx} + \sigma'_{yy}) \quad (22)$$

where ν is Poisson's ratio. Therefore,

$$\sigma_R = \nu \quad (\text{plane - strain}) \quad (23)$$

for a plane-strain linear elastic problem. By the definition of plane-stress, $\sigma'_{zz} = 0$; therefore,

$$\sigma_R = 0. \quad (\text{plane - stress}) \quad (24)$$

It has been shown that the mechanical behavior of polymers depends on their stress, strain, and temperature history. This dependence is characterized by the material clock of the SPEC model. Further, during explicit dynamics calculations, the stress (and displacement) field can become noisy with spurious high frequency oscillations that are a numerical artifact of crack growth. Therefore, we find it beneficial to average σ_R over time. A large number of time averaging schemes for σ_R are possible. In this work, σ_R was averaged over a window of time as

$$\bar{\sigma}_R = \frac{1}{t_2 - t_1} \int_{t_1}^{t_2} \sigma_R dt, \quad (25)$$

where t_1 and t_2 merely represent a window of time in which to average σ_R . The initial time t_1 was taken as the moment that the cohesive traction was 50% of $\hat{\sigma}_{min}$ from Figure 3. The upper bound t_2 was taken to be the current time.

3.6. Coupled Stress State and Rate Effects

The last step in formulating the cohesive zone model is to couple the stress state controlled failure and the rate controlled failure into one parameter. The result of this coupling was that a single fracture mode would be predicted by the model after taking into account the cohesive opening rate and the stress state of the surrounding bulk elements. Recall that the critical opening rate and stress ratio that result in the transition from high to low failure energy are λ_C and σ_{RC} , respectively. The fracture mode is given by the value of P , calculated as

$$P = \left[A \frac{\sigma_R}{\sigma_{RC}} + (1 - A) \frac{\lambda}{\lambda_C} \right], \quad (26)$$

where $0 \leq A \leq 1$ is a separate parameter, determined by the user, which allows for user control regarding how much each critical parameter can affect the fracture mode. Exclusively rate-dependent behavior occurs when $A = 0$. Exclusively stress state-dependent behavior occurs when $A = 1$. In order to investigate the stress-state and rate coupled case, $A = 0.5$ in this work. If P is calculated to be greater than or equal to 1, it is assumed that the low energy criterion will control and fast, brittle failure is expected. This corresponds to either a plane strain stress state or a fast loading rate. Alternatively, $P < 1$ indicates that the specimen is either in plane stress or the loading rate is slow and the high energy criterion will control resulting in slow, ductile failure.

As a summary, the normal cohesive tractions are calculated by

$$\hat{\sigma}_{coh}^n = \begin{cases} \frac{\hat{\sigma}^n}{\delta_1 \Delta_p^n} \Delta_{coh}^n & \text{for } \Delta_{coh}^n \leq \delta_1 \Delta_p^n \\ \hat{\sigma}^n & \text{for } \delta_1 \Delta_p^n < \Delta_{coh}^n < \delta_2 \Delta_p^n \\ \hat{\sigma}^n \left(\frac{1}{1-\delta_2} \right) \left[1 - \frac{\Delta_{coh}^n}{\Delta_p^n} \right] & \text{for } \delta_2 \Delta_p^n \leq \Delta_{coh}^n \leq \Delta_p^n \end{cases} \quad (27)$$

where Δ_{coh}^n is the displacement jump across the cohesive element's normal direction (direction of crack opening), $\hat{\sigma}_{coh}^n$ is the actual traction returned by the cohesive zone, and $\hat{\sigma}^n$ and Δ_p^n are the peak traction and cohesive opening values used in calculations. Those are determined by

$$\begin{aligned} &\text{if } (P \geq 1) \\ &\quad \Delta_p^n = \Delta_{min} \\ &\quad \hat{\sigma}^n = \hat{\sigma}_{min} \\ &\text{else} \\ &\quad \Delta_p^n = \Delta_{max} \\ &\quad \hat{\sigma}^n = \hat{\sigma}_{max}. \end{aligned}$$

4. Initial Boundary Value Problem

In this work, the crack path was specified *a priori*. Therefore, the propagation direction was taken to be the same as the global x direction, the loading direction was the global y direction, and the out of plane direction was the z direction. In this orientation, the in-plane stresses are the σ_{xx} , σ_{yy} , and σ_{xy} components of the stress tensor. The thickness direction axial stress is then σ_{zz} .

Consider an arbitrary cracked domain Ω with natural and kinematic boundary conditions as seen in Figure 6. The boundary of Ω is specified by Γ , with appropriate subscripts defining the surfaces where boundary conditions act on Ω . The dashed boundary Γ_c represents the portion of the geometry ahead of the crack tip where cohesive surfaces are defined. The governing equilibrium equation for the entire body at an instant in time can be written as

$$\int_{\Gamma} \hat{\underline{\sigma}} \, d\Gamma + \int_{\Omega} \rho \underline{b} \, d\Omega = \int_{\Omega} \rho \underline{\ddot{u}} \, d\Omega, \quad (28)$$

where $\hat{\underline{\sigma}}$ are traction vectors, \underline{b} are body forces, and $\underline{\ddot{u}}$ represents the second time derivative of the displacement field, the acceleration. In general, tractions are defined as

$$\hat{\underline{\sigma}} = \underline{\underline{\sigma}} \underline{n}, \quad (29)$$

where \underline{n} is a vector normal to the boundary the traction acts upon which is chosen pointing outward of Ω . Applying the definition of the tractions and the divergence theorem, the equilibrium equation can be recast as a domain integral:

$$\int_{\Omega} \left(\nabla \cdot \underline{\underline{\sigma}} + \rho \underline{b} - \rho \underline{\ddot{u}} \right) d\Omega = 0. \quad (30)$$

From 30, the momentum equation can be extracted:

$$\nabla \cdot \underline{\underline{\sigma}} + \rho \underline{b} - \rho \underline{\ddot{u}} = \underline{0}, \quad (31)$$

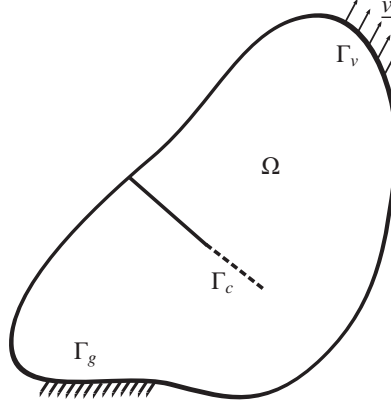


Figure 6: Cracked domain with natural and kinematic boundary conditions. Γ_c represents the cohesive surface.

where $\underline{\underline{\sigma}}$ is the Cauchy stress tensor, determined by (8). The initial boundary value problem consists of finding the displacement field that satisfies the momentum equation subject to initial conditions, natural boundary conditions, and kinematic boundary conditions. The general initial conditions are defined by

$$\begin{aligned} \underline{u}(\underline{x}, 0) &= \underline{u}_0(\underline{x}) & \text{in } \Omega \\ \underline{v}(\underline{x}, 0) &= \underline{v}_0(\underline{x}) & \text{in } \Omega, \end{aligned} \quad (32)$$

where $\underline{v} = \dot{\underline{u}}$ is the velocity. The natural boundary condition is given by

$$\underline{u} = \underline{g} \quad \text{on } \Gamma_g, \quad (33)$$

where g represents a known displacement value on a surface denoted Γ_g . The surface denoted Γ_c represents the cohesive surface. The details of the traction-separation law of the cohesive surface model were presented in Section 3. On Γ_c , the closing traction force can be expressed as a function of the displacement jump Δ_{coh}^n in the normal direction across the cohesive surface as

$$\hat{\underline{\sigma}}_c = \mathcal{F}(\Delta_{coh}^n) \quad \text{on } \Gamma_c. \quad (34)$$

Lastly, a kinematic boundary condition is expressed in terms of velocity which is obtained by differentiating the displacement in time:

$$\dot{\underline{u}} = \underline{v} = \underline{h} \quad \text{on } \Gamma_v \quad (35)$$

where \underline{h} is a velocity value or function of time that is known on the boundary Γ_v .

Combining all these equations, the strong form of the initial boundary value problem can be stated in the following way: given \underline{b} , \underline{g} , \underline{h} , \underline{u}_0 , and $\dot{\underline{u}}_0$, find $\underline{u} : \Omega \times]0, T[\rightarrow \mathbb{R}$ such that

$$(S) \left\{ \begin{array}{ll} \rho \ddot{\underline{u}} = \frac{\partial \underline{\underline{\sigma}}}{\partial \underline{x}} + \underline{b} & \text{on } \Omega \times]0, T[\\ \underline{u} = \underline{g} & \text{on } \Gamma_g \times]0, T[\\ \underline{v} = \underline{h} & \text{on } \Gamma_v \times]0, T[\\ \hat{\underline{\sigma}}_c = \mathcal{F}(\Delta_{coh}^n) & \text{on } \Gamma_c \times]0, T[\\ \underline{u}(\underline{x}, 0) = \underline{u}_0 & \underline{x} \in \Omega \\ \dot{\underline{u}}(\underline{x}, 0) = \dot{\underline{u}}_0(\underline{x}) & \underline{x} \in \Omega \end{array} \right. , \quad (36)$$

where $]0, T[$ represents the open interval of time from 0 to final time T . The weak form of the equation of motion can be obtained by multiplying (31) by a vector-valued test function \underline{w} that represents the virtual change in displacement. Then integrating over the domain of the body and applying the product rule and the divergence theorem to give

$$0 = \int_{\Omega} \underline{\underline{\sigma}} \nabla \underline{w} d\Omega + \int_{\Omega} \rho \ddot{\underline{u}} \underline{w} d\Omega$$

$$\begin{aligned}
& - \int_{\Omega} \underline{b} \delta \underline{w} \, d\Omega - \int_{\Gamma_{ext}} \underline{\hat{\sigma}} \underline{w} \, d\Gamma \\
& - \int_{\Gamma_c} \underline{\hat{\sigma}}_c \llbracket \underline{w} \rrbracket \, d\Gamma,
\end{aligned} \tag{37}$$

where the last integral term is the contribution to the weak form from the cohesive surface Γ_c arising from the cohesive opening Δ_{coh} and Γ_{ext} refers to the external boundary of Ω , or all boundaries except Γ_c . That is,

$$\Gamma = \Gamma_c \cup \Gamma_{ext}. \tag{38}$$

Introducing the standard Finite Element discretization gives rise to the element matrix problem:

$$\underline{\underline{M}}_e \ddot{\underline{d}}_e + \underline{F}_e^{int} = \underline{F}_e^{ext}, \tag{39}$$

where the subscript e represents the matrix or vector on the element level,

$$\underline{\underline{M}}_e = \int_{\Omega_e} \rho \underline{N}^T \underline{N} \, d\Omega \tag{40}$$

is the consistent mass matrix,

$$\underline{F}_e^{int} = \int_{\Omega_e} \underline{B}_e^T \underline{\sigma} \, d\Omega - \int_{\Gamma_c} \underline{N}_e^T \underline{\hat{\sigma}}_c \, d\Gamma \tag{41}$$

describes the element internal force vector, and

$$\underline{F}_e^{ext} = \int_{\Omega_e} \underline{N}_e^T \underline{b} \, d\Omega + \int_{\Gamma_{ext}} \underline{N}_e^T \underline{\hat{\sigma}} \, d\Gamma \tag{42}$$

describes the elemental external force vector. The \underline{N}_e are matrices containing the finite element shape functions and \underline{B}_e are matrices containing the spatial derivatives of the shape functions. The external tractions arising from the cohesive surface on Γ_c can be evaluated by the traction separation law given by (27). The elemental equations are assembled to give rise to the global matrix problem: given $\underline{F} :]0, T[\rightarrow \mathbb{R}^{n_{eq}}$, find $\underline{d} :]0, T[\rightarrow \mathbb{R}^{n_{eq}}$ such that

$$\begin{aligned}
\underline{\underline{M}} \ddot{\underline{d}} &= \underline{F}^{ext} - \underline{F}^{int} & t \in]0, T[\\
\underline{\dot{d}}(0) &= \underline{\dot{d}}_0 \\
\underline{d}(0) &= \underline{d}_0.
\end{aligned} \tag{43}$$

This system was then solved using an explicit time integration scheme with a lumped mass matrix. The next section will detail the numerical analyses performed using the bulk and cohesive zone constitutive models detailed in this section.

5. Numerical Analysis and Discussion

5.1. Problem Setup

Figure 7 shows the single edge notch tension (SENT) geometry simulated by finite element analysis. The SENT geometry was chosen for a simple set up in which to perform the parameter study. In this work, the crack path was specified *a priori* along the surface Γ_c . Three-dimensional simulations were performed on samples ranging from 1 to 4 mm in thickness. The top portion of the specimen represents Γ_v . A vertical (positive y direction) velocity ranging from 8000 mm/min to 500 mm/min was specified on this boundary. This loading rate range gives a corresponding mean strain rate range of $13.333 \, \text{s}^{-1}$ to $0.833 \, \text{s}^{-1}$. The bottom surface of the specimen represents Γ_g . That surface was

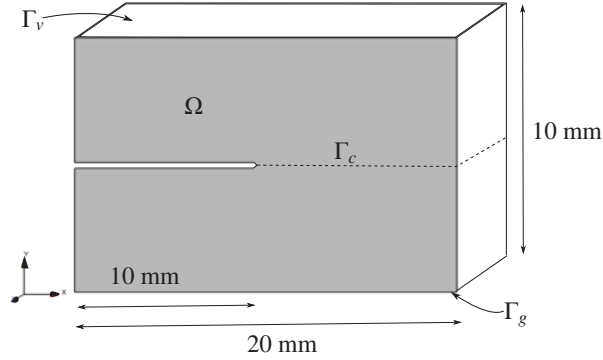


Figure 7: SENT domain with natural and kinematic boundary conditions. The crack path was specified *a priori* along Γ_c . A prescribed velocity was placed on Γ_v and displacement was fixed on Γ_g .

fixed in the vertical (y) direction. Both Γ_v and Γ_g were fixed in the x and z directions in all simulations. Lastly, the dotted horizontal line through the center of the specimen denotes the cohesive surface portion of the boundary Γ_c .

Using the SPEC model, bulk deformation depends upon the thermal and strain history of the material. The thermal history is defined from an initial reference state at a reference temperature. In accordance with Adolf et al. (2009), the reference temperature used for polycarbonate is 423 K and is above the glass transition temperature. The material must be cooled in the simulation to the test temperature (i.e., room temperature). This occurs (similarly to annealing) over a rather large time frame. As suggested by Chambers (2010), that time was taken to be 8500 seconds. Therefore, the first 8500 seconds of the simulation were designated only for a thermal cool down and were performed in a quasi-static sense with inertial effects neglected. This allowed for much larger time stepping. After the cool down was completed, the specimens were loaded by the boundary conditions discussed in the previous paragraph with inertial effects considered in an explicit dynamic scheme. The SPEC model parameters used in this study were taken from Adolf et al. (2009) and are listed in Table 1.

5.2. High vs. Low Energy Failure - TH Model Parameter Study

Recall that the new CZM implemented in this work is derived from the model developed by Tvergaard and Hutchinson (1992). If $\hat{\sigma}_{min} = \hat{\sigma}_{max}$ and $\Delta_{min} = \Delta_{max}$, then that model is exactly recovered. It is then possible to perform a parameter study on $\hat{\sigma}$ and Δ to specify how different failure energies affect crack growth in simulations.

As discussed earlier, the works of Wolstenholme et al. (1964), Ravetti et al. (1975), Broutman and Krishnakumar (1976), Yee (1977), and Selden (1987) provide some insight into the amount of energy required per unit area of crack advance in PC. All of the mentioned works, excepting Selden (1987), were performed on impact tests. In impact tests, the energy per unit area of crack growth reported is in the range of 1.5×10^3 to 7.0×10^3 N-m/m² for brittle failures and in the range of 52.0×10^3 to 70.0×10^3 N-m/m² for ductile failures. Selden (1987) performed failure analysis on compact tension specimens and reported failure energy per unit area of crack advance to be in the range of 1.5×10^3 to 2.6×10^3 N-m/m² for brittle failures and in the range of 12.3×10^3 to 14.9×10^3 N-m/m² for ductile failures. While test setup plays a role in the failure energy, the important conclusion is that brittle or fast fracture results in a minimal energy per unit area of crack growth while ductile or slow failure results in a much higher energy per unit area of crack growth.

Using these works as a baseline for crack growth, the parameters for fast fracture were $\hat{\sigma}_{min} = 50$ MPa and $\Delta_{min} = 8 \times 10^{-5}$ m. These values resulted in a cohesive energy for failure of 3.8×10^3 N-m/m². The first value was physically intuitive since 50 MPa is near, but not over, the yield stress of polycarbonate and brittle failure is expected to occur with minimal finite strain deformation. The value of Δ_{min} was chosen so that the cohesive energy would be in the expected range for brittle crack growth. The subsequent values used to represent the high energy or ductile failure scenario were $\hat{\sigma}_{max} = 106$ MPa and $\Delta_{max} = 3.0 \times 10^{-4}$ m. A parameter study not shown here led to these values. In this case, $\hat{\sigma}_{max}$ was set high enough to force large strain deformations in the surrounding bulk material. It was expected *a priori* that slow crack growth would manifest itself by allowing a finite amount of crack extension

Table 1: Parameters values of the SPEC model

Parameter	Value	Units
T_{ref}	423.15	°Kelvin
$K_{\infty}(T_{ref})$	3.2	GPa
$K_g(T_{ref})$	4.9	GPa
$\alpha_{\infty}(T_{ref})$	0.00058	ppm/°C
$\alpha_g(T_{ref})$	0.000185	ppm/°C
$d\alpha_{\infty}/dT$	6e-7	ppm/°C ²
$d\alpha_g/dT$	1e-7	ppm/°C ²
$G_{\infty}(T_{ref})$	1	Pa
$G_g(T_{ref})$	0.65	GPa
dG_{∞}/dT	0.0	GPa/°C
dG_g/dT	-0.2	MPa/°C
C_1	12	-
C_2	42	°C
C_3	2000	°C
C_4	15000	°C/Pa
τ_v	20	s ⁻¹
β_v	0.15	-
τ_s	0.15	s ⁻¹
β_s	0.38	-

(approximately one to three elements), then some time would pass without crack growth. Stress would then build in the specimen before more cohesive failure would occur. The crack would continue to progress in this start/stop mechanism through the entire specimen. The parameters chosen for Δ_{max} and $\hat{\sigma}_{max}$ represent the first instances where the crack growth proceeded in an obvious start/stop manner. The cohesive energy associated with failure in this case with the parameters mentioned was 30.2×10^3 N-m/m². For completeness, $\delta_1 = 0.05$ and $\delta_2 = 0.95$ in this work.

As a parameter study, the values for $\hat{\sigma}_{max}$ and Δ_{max} can be placed into the TH model to yield a slow crack growth scenario. Alternatively, the parameter values for $\hat{\sigma}_{min}$ and Δ_{min} can also be introduced to yield a fast crack growth scenario. Figure 8 displays the instantaneous crack velocity as a function of crack position for the fast case and the slow case. The total work per unit area of crack growth was evaluated for the entire simulation by taking the area under the global load-displacement curve seen in Figure 9. It was found to be 3.9×10^3 N-m/m². Accounting for bulk elastic deformations increased the energy required for crack growth, by about 3%. The total work per unit of crack growth is still well within the range specified by the earlier referenced works. The total time for crack growth in the slow case is about 1.0×10^{-3} s and about 40.0×10^{-6} s in the fast growth case.

Table 2 summarizes the findings of the CZM model parameter study used to parameterize the rate and stress state dependent cohesive zone model for this work.

Table 2: Summary of parameter study of CZM model behavior for fast and slow failure.

	Low Energy	High Energy
$\hat{\sigma}$ (MPa)	50	106
Δ (m)	8×10^{-5}	3×10^{-4}
max vel (m/s)	488	150
avg vel (m/s)	214	9
E_{coh} ($\times 10^3$ N-m/m ²)	3.8	30.2
E_{tot} ($\times 10^3$ N-m/m ²)	3.9	34.5
ϵ_{max} (% in bulk)	3	7

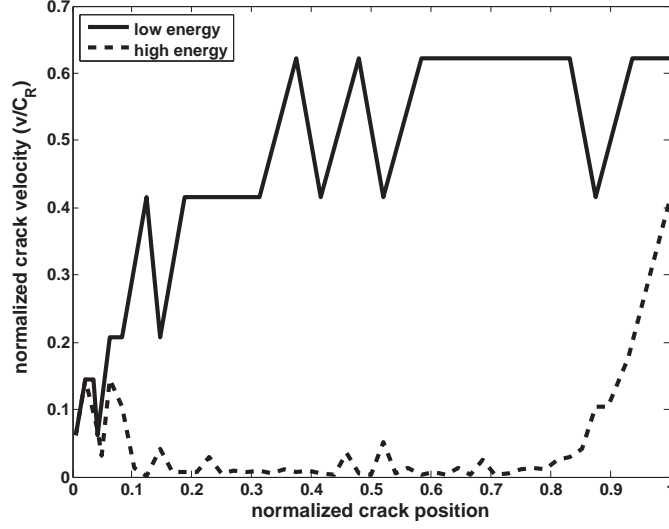


Figure 8: Fast and slow crack velocities with TH model. In the low energy case, crack velocity builds to greater than 1/2 the Rayleigh wave speed, or 488 m/s. Crack velocity averages about 7.6 m/s with a peak of 22.8 m/s in the middle portion (normalized crack position between 0.1 and 0.8) of the slow crack growth scenario. Velocity is calculated by the distance the crack has advanced since the last instance of crack advance divided by the difference in time between the two crack growth occurrences.

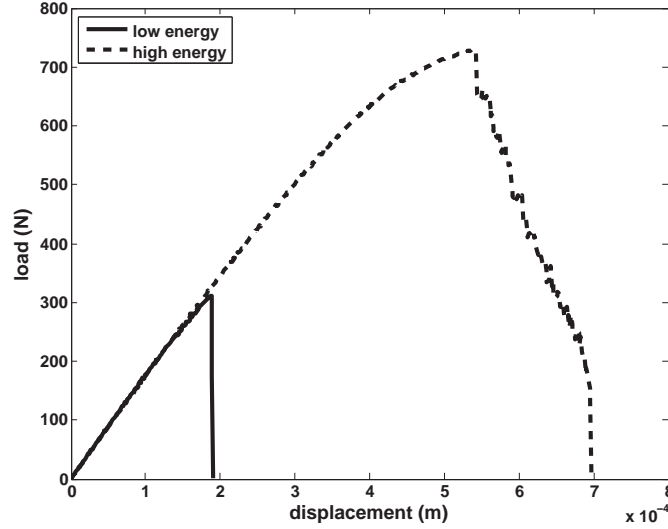


Figure 9: Load-displacement plots for fast and slow crack growth cases. The energy for failure was 3.9×10^3 N-m/m² in the fast growth case and 34.5×10^3 N-m/m² in the slow growth case.

5.3. Rate-Controlled Crack Growth

During rate dependent simulations, the parameter A of (26) was set to be equal to zero. Rate effects were investigated using a thin (1 mm in thickness) geometry since thickness effects were not important. Table 3 shows the predicted fracture mode with only rate dependence considered by the cohesive zone model. As the loading rate (units of mm/min) is decreased, it is expected that more ductile or slow failures will occur. For any given value of λ_C ,

this is the case. The key feature of this model is the ability to capture the energy for failure required under different fracture modes. Conventional wisdom indicates that strain-rate sensitive materials harden with increases in loading rate. However, implementation of this behavior typically is performed by constructing a cohesive zone model that returns a higher traction value at increased loading rates. This results in higher energy values for failure, which is not consistent with the results reported earlier by Wolstenholme et al. (1964), Ravetti et al. (1975), Broutman and Krishnakumar (1976), Yee (1977), and Selden (1987). Rather, this work simply enforces a lower overall energy for failure that corresponds to the worst-case scenario at high cohesive opening rates above λ_C . This logic has the ability to capture the rate dependent fracture mode transition seen in the laboratory in PC.

Table 3: Rate dependence of new cohesive zone in fracture simulations.

λ_C	Loading Rate (mm/min)		
	8000	4000	2000
2.40×10^5	fast	fast	fast
2.45×10^5	fast	fast	fast
2.46×10^5	fast	fast	slow
2.47×10^5	fast	fast	slow
2.50×10^5	fast	fast	slow
2.51×10^5	fast	fast	slow
2.52×10^5	fast	slow	slow
2.55×10^5	fast	slow	slow
2.56×10^5	slow	slow	slow
2.58×10^5	slow	slow	slow

Figure 10 shows the crack velocities predicted when $\lambda_C = 2.45 \times 10^5$. For this value of λ_C , all the loading rates resulted in fast crack growth. Conversely, in Figure 11, $\lambda_C = 2.56 \times 10^5$ results in all the loading rates yielding slow, stable crack growth. It appears that the predicted crack growth velocity is dependent on the loading rate in the slow crack growth case. This behavior is expected because in slow crack growth a few elements open immediately, then an amount of time passes before the stress can build up enough to open a few more elements. A faster loading rate simply results in less time to build the stress to the required levels for failure. No differences were seen in the crack growth at a single loading rate, with different values of λ_C , if the same fracture mode was expected. For example, at a loading rate of 4000 mm/min, if $\lambda_C \geq 2.52 \times 10^5$, all crack growths were slow and identical.

5.4. Stress-Controlled Crack Growth

5.4.1. Preliminaries

As mentioned in Section 1, the stress state of the material has a great influence on the fracture mode expected. Adding the stress state dependence of (21) is a major contribution of this work. Siegmund and Brocks (2000), Tijssens et al. (2000), Estevez et al. (2000), Gearing and Anand (2004), and Anvari et al. (2006) are some authors that have used information from the stress state in finite element simulations of material failures. With the exception of Gearing and Anand (2004) all of these works are limited to two dimensions. Only Siegmund and Brocks (2000) and Anvari et al. (2006) use information from the bulk field's stress state to inform the cohesive zone model's behavior. However, their use of stress triaxility in two dimensions misses the most important aspect of the stress state: the out of plane stress (i.e., σ_{zz}). Table 4 illustrates this point. In these simulations, two specimens of different thicknesses (1 mm and 6 mm) were loaded to the same displacement prior to cohesive crack growth. The third column corresponds to a 1mm thick sample with a highly refined mesh. That result will be discussed shortly. The stress states of the bulk material were analyzed to determine the effects that thickness has on the stress state. It was found that the in-plane components (x and y) were remarkably consistent even as thickness changed. However, there is a significant change in the z component stress values. If stress state is to be used in numerical analysis to determine fracture mode, then three dimensional simulations must be used in order to capture the effects the out-of-plane stresses. This is especially important when investigating the transition from plane strain to plane stress or from fast to slow failure because the

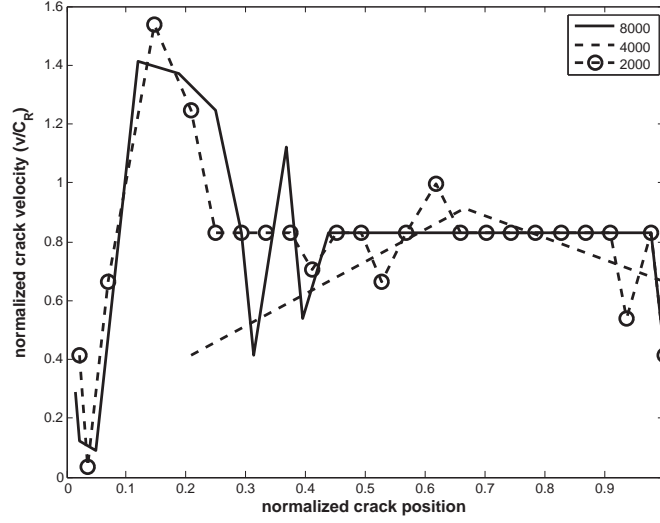


Figure 10: Comparison of fast crack growth velocities at different loading rates. ($\lambda_C = 2.45 \times 10^5$)

Table 4: Maximum stress values in meshes of two different thicknesses

$\sigma (MPa)$	6 mm	1 mm	1mm-fine
σ_{xx}	28	28	35
σ_{yy}	51	51	51
σ_{zz}	18	5	9
σ_{xy}	20	20	25
σ_{xz}	10	2.8	3.9
σ_{yz}	11.7	4.7	7

stress state in a three dimensional specimen is a combination of plane strain in the interior and plane stress at the exterior of the geometry.

Figures 12 and 13 show the effect of thickness on σ_R in simulations. The ratio σ_R calculated from (21) is a natural way to determine how “close” a portion of the geometry is to a plane stress or a plane strain stress state. The figure displays the plane in which a crack would propagate. The black line represents the crack front with the arrows pointing in the direction of crack growth. The area immediately ahead of the crack tip experiences a maximum σ_R value of 0.22 in the 6 mm sample; the 1 mm sample exhibits a maximum σ_R of 0.062. This shows that there is a quantitative difference between σ_R in specimens of different sample thicknesses. These meshes are identical with the exception that Figure 12 is six times the thickness of Figure 13. The element sizes are all identical. This results in a rather coarse mesh for the 1 mm geometry.

To investigate the effect that mesh refinement has on σ_R , the 1 mm thick sample was refined to an element height three times smaller than that seen here. Therefore, there were 18 elements through the thickness instead of 6 as shown in the figure. Figure 14 shows the σ_R response of the finer 1 mm mesh. The σ_R scale is the same as the 6 mm mesh from earlier. Notice that there is an obvious quantitative difference between the σ_R values in each geometry. The peak σ_R in the fine mesh is about 0.12. These values correspond to a percent difference of about 83%. The mesh refinement leads to a slight change in the stress tensor as seen in Table 4. Additionally, consider the stress criterion of a critical hydrostatic stress being used to determine if plane stress or plane strain controls. Recall that hydrostatic stress is defined as

$$\sigma_H = \frac{1}{3}(\sigma_{xx} + \sigma_{yy} + \sigma_{zz}). \quad (44)$$

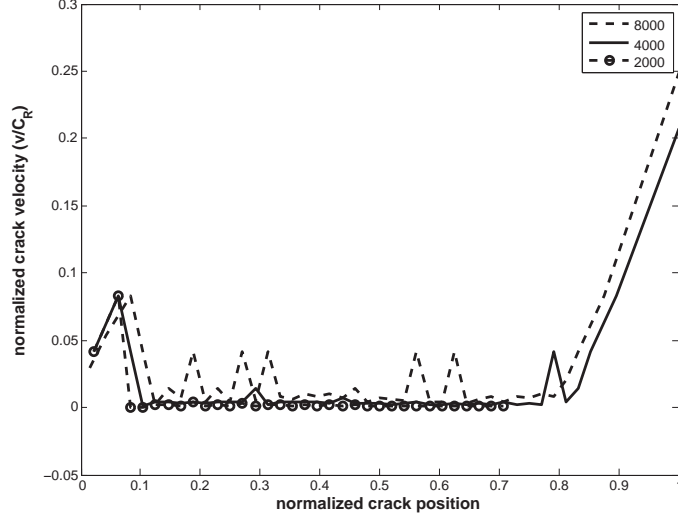


Figure 11: Comparison of slow crack growth velocities at different loading rates. ($\lambda_C = 2.56 \times 10^5$)

From Table 4, the σ_H value for each mesh is 97, 84, and 95 MPa respectively. There appears to be a difference between the 1mm and 6mm thick geometries; that difference is about 15% initially for the same level of discretization. However, when the 1mm mesh is refined, that difference quickly disappears.

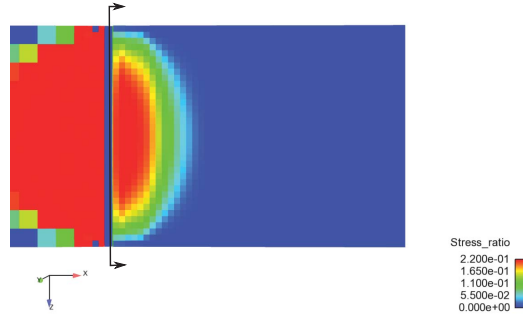


Figure 12: Stress ratio (σ_R) in 6 mm sample.

In the previous example, σ_R was evaluated by analyzing the bulk elements that border cohesive elements. It is necessary to inform the cohesive zone elements with σ_R from the surrounding bulk elements to perform this type of analysis. As an example, consider a cohesive element that is bordered by two adjacent bulk elements in a three-dimensional mesh as seen in Figure 15. During the cohesive surface initialization, the bulk element global identification numbers were determined by searching the mesh for shared nodes. For the given example, this process would determine that cohesive element #3 is attached to bulk elements #1 and #2. When cohesive element #3 is instructed to provide its traction value for the internal force vector, the current stress of state of elements #2 and #1 are processed to return a σ_R^e value for each element. Then, both σ_R^e values are averaged to return the average bulk stress ratio σ_R actually experienced by the cohesive surface element. This value is then passed to the cohesive surface model routine to determine whether a high or low energy threshold should be used in the calculation.

The method implemented to return σ_R is only valid if no topological mesh changes occur during the simulation. That is the case for the simulations run in this work. However, if cohesive surface elements were to be dynamically inserted into the mesh, the search for bordering elements would have to be performed just before calculating the



Figure 13: Stress ratio (σ_R) for coarse mesh in 1mm sample.



Figure 14: Stress ratio (σ_R) for fine mesh in 1mm sample.

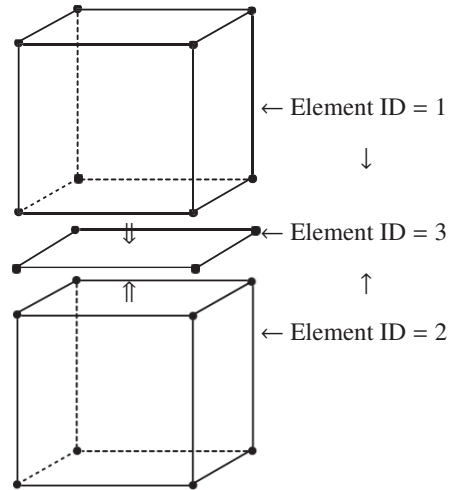


Figure 15: Cohesive surface element inserted between two bulk finite elements. The cohesive surface relies on stress state information from the surrounding bulk elements to determine the failure energy required.

internal force vector, not during the initialize step. This would result in significant reductions in a finite element code's performance.

5.4.2. Stress Dependent Cohesive Zone Results

In order to elucidate the stress state dependence of the model, the σ_R term was isolated by placing $A = 1$ in (26). Simulations were performed in the same manner as in the rate dependent case. In this parameter study, σ_{RC} was varied as was the specimen thickness. This resulted in determining of σ_{RC} values where each specimen thickness transitions from slow to fast fracture.

Table 5: Stress dependence of new cohesive zone in fracture simulations

σ_{RC}	1 mm	2 mm	3 mm
0.007	fast	fast	fast
0.008	trans	fast	fast
0.009	trans	trans	fast
0.010	slow	trans	fast
0.011	slow	trans	fast
0.012	slow	trans	trans
0.013	slow	slow	trans
0.014	slow	slow	slow
0.015	slow	slow	slow
0.016	slow	slow	slow

Table 5 shows the results of the σ_{RC} and thickness parameter study. The fracture modes “fast” and “slow” are defined in the same way as the previous section. However, now there is a separate fracture mode termed “trans” for transition. The transition fracture mode indicates that one particular type of fracture mode did not dominate the entire fracture. For example, in some cases a crack would progress slowly for some time, then quickly through the remainder of the specimen. If the slow crack growth portion was less than 1/2 of the specimen fracture area, fast crack growth was said to be the controlling mode. In simulations, if fast fracture would occur after 1/2 of the total area of crack growth had occurred, then the failure was called a transition failure. The one exception to this occurred when the last few elements near the end wall would quickly fail. This was called slow fracture because the speed of the crack advance was overwhelmingly slow and the failure energy was obviously high energy, but only the last 3-6 rows of elements would quickly open. This slow behavior was explained earlier and can clearly be seen in Figure 8

Figure 16 shows the simulated fracture velocities of a fast, transition, and slow failure in a 2 mm thick sample using the stress controlled cohesive zone model. The stress controlled fast and transition failures show a period of slower velocity crack growth at the beginning of the fracture. This period seems to correspond very well to zone I of PC’s fracture surface morphology characterized by Hull and Owen (1973). During that time, stress builds and the crack progresses slowly in a relative thumbnail shape. Eventually, in the transition or fast cases, the crack will begin to progress quickly. In the slow cases, it continues to slowly progress.

An example of the thumbnail shaped crack can be seen in Figure 17, which shows a 2 mm thick specimen near the end of zone I, just before the crack progresses quickly. The top half of the specimen is removed so that the cohesive zone elements along the plane of crack growth may be viewed. The bottom half of the specimen is colored by the maximum principal stress values per element. The cohesive elements are colored gray and are set to disappear after cohesive death has occurred. This enables the visualization of the crack tip as it advances.

If a single σ_{RC} value is considered, like 0.011, it is easy to see that a transition in fracture mode occurs as the specimen thickness is increased. In the next section, stress state and rate effects will be coupled to simulate a fracture mode transition with both effects considered simultaneously.

5.5. Coupled Rate and Stress Effects

The coupling of rate and stress state effects by (26) is the key feature of this model. The final parameters investigated in this study were $A = 0.5$, $\sigma_{RC} = 0.0065$, and $\lambda_C = 2.50 \times 10^5$. Table 6 shows the results for fracture mode for the material parameters given.

The parameters σ_{RC} and λ_C were chosen with time constraints in mind. That is, σ_{RC} was chosen lower than the expected value, based on the study from Section 5.4.2. This allowed for the transition from ductile to brittle failure

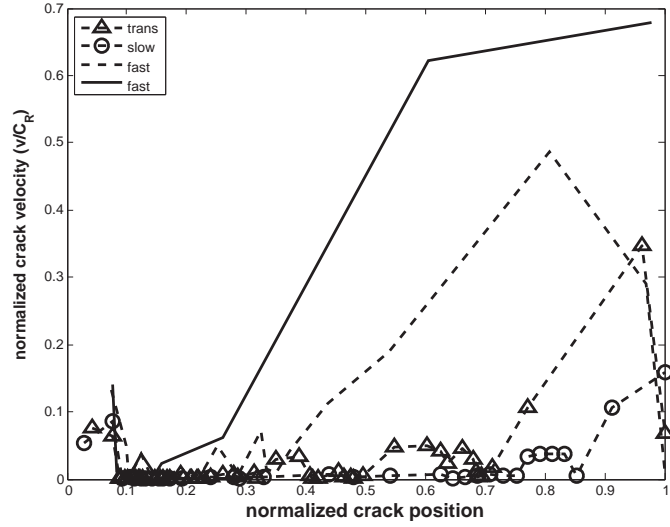


Figure 16: Simulated fracture velocities with stress controlled cohesive zone. The crack velocity transitions from fast to slow as σ_R is adjusted to require a stress state approaching plane strain for low energy failure.

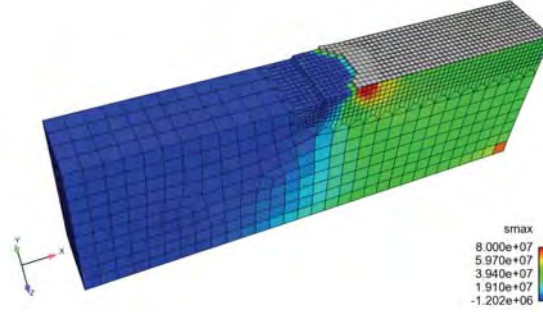


Figure 17: Zone I and a thumb-nail-shaped crack front in a finite element simulation.

to occur at a lower value of thickness. Therefore, fewer total elements were needed in simulations. For example, all other things remaining equal, a mesh that is 1 mm in thickness will have three times fewer elements than a mesh that is 3 mm in thickness. This explains the very minor changes in the fracture mode results at thicknesses greater than 2 mm. Likewise, λ_C was chosen in such a way as to minimize simulation time. This resulted in an arbitrarily large value for the parameter, but allowed for a fracture mode transition to occur at higher overall loading rates. In explicit dynamics, the time step size is limited for solution stability. Therefore a simulation run with an 8000 mm/min loading rate actually takes about eight times shorter to run than a simulation with a 1000 mm/min loading rate. To further appreciate the time constraints mentioned above, a 1 mm thick sample loaded at 8000 mm/min had a run time of just over 7 hours when run on 16 processors of the MPI cluster used in this work.

In summary, the data of Table 6 display unprecedented results. Consider the fast fracture mode of the 1 mm thick geometry loaded at 8000 mm/min. Due to thickness, it would be expected that a 1 mm sample is very nearly in a plane-stress stress-state and slow fracture would be expected. However, due to the fast loading rate dominating in the controlling equation (26), the sample fails in a brittle manner. This is consistent with the behavior seen in thin samples of PC. As the loading rate is decreased (e.g., 6000 mm/min), the fracture mode transitions into the slow regime. This

Table 6: Fracture mode transition for coupled problem.

Loading Rate	1 mm	2 mm	3 mm	4 mm
8000	fast	fast	fast	fast
7800	fast	fast	fast	fast
7600	fast	fast	fast	fast
7500	slow	fast	fast	fast
7000	slow	fast	fast	fast
6000	slow	fast	fast	fast
5000	slow	fast	fast	trans
4000	slow	trans	trans	trans
2000	slow	trans	trans	trans
1000	slow	trans	slow	trans
500	slow	slow	slow	slow

allows for the stress-state in the material ahead of the crack tip to control the failure mode. Then as the thickness is increased, but loading rate is held constant, the fracture mode transitions back to fast fracture. This occurs because the stress-state has been increased toward a plane-strain stress-state. This is the first instance of using numerical analysis to simulate a fracture mode transition due to rate and thickness effects with a single set of material input parameters.

6. Conclusions

In this work, the SPEC model has been applied to mode I fracture problems in thermoplastic glassy polymers. The model is a continuum model; therefore, it is not designed to capture the different micromechanical processes, such as crazing, that influence the deformation behavior of the material. However, the new cohesive zone model was implemented to phenomenologically capture the micromechanical processes in the fracture process zone that the SPEC model was not designed to capture.

A single set of input parameters have been used to simulate the transition from slow to fast fracture as both thickness and loading rate change. Three-dimensional explicit dynamic finite element analysis was performed and a new cohesive zone model was implemented that is rate and stress state dependent. Therefore, loading rate and thickness inform the traction-separation behavior. The cohesive zone model's behavior accounts for both the low energy critical scenario of fast, brittle crack growth and the high energy scenario of slow, ductile crack growth. While there are some rate dependent and/or stress dependent cohesive models, these models either are not applicable to polymer behavior, or are not capable of capturing a fracture mode transition.

In this work, the cohesive traction remains constant in areas of either ductile or brittle failure and reduces from high to low as loading rate is increased. This results in less bulk yielding at high loading rates and thus more fast, brittle failures. The rate dependence of the cohesive model is incorporated by determining the cohesive opening rate. The model uses a critical cohesive opening rate λ_C as the threshold opening rate. Below λ_C , the high energy regime controls, resulting in slow, ductile failure. Above λ_C , the low energy regime controls, resulting in fast, brittle failure.

Three-dimensional analysis is of primary importance when performing stress analysis aimed at the ductile to brittle transition. Plane-strain results in fast, brittle failure and plane-stress results in slow, ductile failure. Two-dimensional analysis idealizes stress in the third dimension. Previous stress state dependent cohesive zone models are limited by two-dimensional analysis.

Here we show that regardless of thickness, in-plane stresses do not vary significantly. However, the stress in the thickness direction varies significantly. A stress ratio σ_R was proposed that is able to quantify the amount of plane-strain or plane-stress that exists at a point. A critical σ_{RC} was utilized above which the low energy regime controlled crack growth and above which the high energy regime controlled crack growth.

The stress and rate dependencies were coupled in a simple, linear way. Without changing input parameters, the model shows a fast, brittle failure in a thin sample thickness when loaded at a high loading rate. As the loading rate is reduced, the model transitions to slow, ductile crack growth. As the sample thickness is increased, while holding

loading rate constant at the lower value, the model transitions back to the fast crack growth regime. This behavior is consistent with the behavior seen in the experimental analysis. The model can easily be used and compared with experimental results to construct the full fracture mode transition behavior based on loading rate and thickness effects.

References

- Adolf, D., Chambers, R., Neidigk, M., 2009. A simplified potential energy clock model for glassy polymers. *Polymer* 50, 4257–4269.
- Anvari, M., Scheider, I., Thaulow, C., 2006. Simulation of dynamic ductile crack growth using strain-rate and triaxiality-dependent cohesive elements. *Engineering Fracture Mechanics* 73, 2210–2228.
- Banerjee, A., Manivasagam, R., 2009. Triaxiality dependent cohesive zone model. *Engineering Fracture Mechanics* 76, 1761–1770.
- Barenblatt, G., 1959. The formation of equilibrium cracks during brittle fracture. general ideas and hypotheses. axially-symmetric cracks. *Applied Mathematics and Mechanics (PMM)* 23, 434–444.
- Brouman, L., Krishnakumar, S., 1976. Impact strength of polymers: 1. the effect of thermal treatment and residual stress. *Polymer Engineering and Science* 16, 74–81.
- Caruthers, J., Adolf, D., Chambers, R., Shrikhande, P., 2004. A thermodynamically consistent, nonlinear viscoelastic approach for modeling glassy polymers. *Polymer* 45, 4577–4597.
- Chambers, R., 2010. personal communication.
- Dugdale, D., 1960. Yielding of steel sheets containing slits. *Journal of Mechanics and Physics of Solids* 8, 100–104.
- Estevez, R., Tjssens, M., van der Giessen, E., 2000. Modeling of the competition between shear yielding and crazing in glassy polymers. *Journal of Mechanics and Physics of Solids* 48, 2538–2617.
- Gearing, B., Anand, L., 2004. On modeling the deformation and fracture response of glassy polymers due to shear-yielding and crazing. *International Journal of Solids and Structures* 41, 3125–3150.
- Hull, D., Owen, T., 1973. Interpretation of fracture surface features in polycarbonate. *Journal of Polymer Science: Polymer Physics Edition* 11, 2039–2055.
- Ishikawa, M., Narisawa, I., H., O., 1977. Criterion for craze nucleation in polycarbonate. *Journal of Polymer Science: Polymer Physics Edition* 15, 1791–1804.
- Kambour, R., 1973. A review of crazing and fracture in thermoplastics. *Journal of Polymer Science: Macromolecular Reviews* 7, 1–154.
- Kramer, E., 1984. Craze fibril formation and breakdown. *Polymer Engineering and Science* 24, 761–769.
- Moes, N., Dolbow, J., Belytschko, T., 1999. A finite element method for crack growth without remeshing. *International Journal of Numerical Methods in Engineering* 46, 131–150.
- Ravetti, R., Gerberich, W., Hutchinson, T., 1975. Toughness, fracture markings, and losses in bisphenol-a polycarbonate at high strain-rate. *Journal of Materials Science* 10, 1441–1448.
- Scheider, I., Rajendran, M., Banerjee, A., 2011. Comparison of different stress-state dependent cohesive zone models applied to thin-walled structures. *Engineering Fracture Mechanics* 78, 534–543.
- Selden, R., 1987. Fracture energy measurements in polycarbonate and pmma. *Polymer Testing*, 209–222.
- Siegmund, T., Brocks, W., 2000. A numerical study on the correlation between the work of separation and the dissipation rate in ductile fracture. *Engineering Fracture Mechanics* 76, 139–154.
- Tijssens, M., van der Giessen, E., Sluys, L., 2000. Modeling of crazing using a cohesive surface methodology. *Mechanics of Materials* 32, 19–35.
- Tvergaard, V., Hutchinson, J., 1992. The relation between crack growth resistance and fracture process parameters in elastic-plastic solids. *Journal of Mechanics and Physics of Solids* 40, 1377–1397.
- Wolstenholme, W., Pregon, S., Stark, C., 1964. Factors influencing izod impact properties of thermoplastics measure with the autographic impact test. *Journal of Applied Polymer Science* 8, 119–140.
- Yee, A., 1977. The yield and deformation behaviour of some polycarbonate blends. *Journal of Materials Science* 12, 757–765.
- Zhang, Z., Paulino, G., Celes, W., 2007. Extrinsic cohesive modelling of dynamic fracture and microbranching instability in brittle materials. *International Journal for Numerical Methods in Engineering* 72, 893–923.